Nuclear-wave-packet dynamics mapped out by two-center interference in the HeH^{2+} molecule

M. Schüler, Y. Pavlyukh, and J. Berakdar*
Institut für Physik, Martin-Luther-Universität Halle-Wittenberg, 06120 Halle, Germany
(Received 18 February 2014; published 30 June 2014)

Photoemission from diatomic molecules closely resembles the Young-type double-slit experiment where each of the two atomic sites represents a coherent emission source. When the photoelectron wavelength becomes commensurate with the effective interatomic distance, the resulting spatial interference gives rise to oscillations in the photoionization total and differential cross sections. This phenomenon provides detailed information on the molecular geometry, a fact that can be utilized for probing the nuclear dynamics triggered by the interaction with a laser field. We demonstrate how this coherent wave-packet evolution can be traced by observing the photoelectron angular distribution. Based on *ab initio* scattering calculations we perform a proof-of-principle reconstruction of the nuclear-wave-packet evolution in the HeH^{2+} molecule.

DOI: 10.1103/PhysRevA.89.063421 PACS number(s): 33.80.Be, 33.60.+q, 31.15.A−, 73.22.Dj

I. INTRODUCTION

The impressive experimental advance over recent years in generating ultrashort, high-energy coherent x-ray laser pulses enabled new insight in the electronic structure of extended solid-state systems, large biomolecules down to small molecules, and atoms, allying submolecular spatial with femtosecond temporal resolution [1–6]. In particular, the x-ray absorption (XAS) reveals detailed structural information, especially at the photon energy high enough to eject a core electron to the continuum. The subsequent multiple scattering of the photoelectron from the neighboring atoms and its interference gives rise to an oscillatory behavior of the x-ray absorbance, known as extended x-ray absorption fine structure, whose period is directly related to the structural arrangement of the sample [7,8].

Similar interference effects have also been predicted for the photoemission cross section of diatomic molecules [9], highlighting the analogy to the Young-type double-slit experiment. However, due to the typically smaller internuclear distance, tracing those oscillations has been a challenge, for it requires tuning the photon energy over several hundred electron volts [10–14]. Moreover, the hybridization of the atomic wave functions into molecular states gives rise to new effects, such as oscillations in the *angle-resolved* distribution of the emitted electrons as a function of energy, as well. The photoelectron angular distribution (PAD) strongly depends on the parity of the electron wave function and thus contains the signature of the respective angular momentum [14] or exhibits asymmetries due to the superposition of gerade and ungerade states [15,16].

On the other hand, diatomic molecules are convenient testing systems where important insights [17–19] in the nuclear dynamics can be gained either by means of (e.g., two-color) pump-probe techniques [20–22] or by recolliding electrons giving rise to higher harmonics generation [23]. For both scenarios, the fragmentation of the molecule after electron ejection by an ultrashort laser pulse—the Coulomb explosion (CE)—provides rich information on the initial or excited molecular configuration and even allows for reconstructing the corresponding nuclear wave packet (NWP) [17,20–22,24,25]. Mapping out the NWP can be ambiguous for more complex targets due to the variety of accessible electronic channels; additionally measuring the PAD narrows down the number of pathways and improves the NWP reconstruction [25].

The simplest systems proving this kind of physics are the homonuclear dihydrogen cation H_2^+ and the heteronuclear helium hydrogen double cation HeH^{2+}. Whereas the former allows for investigating the interference from identical atoms [26–28], the HeH^{2+} system provides an example of interference from different emission centers [29,30]. From the theoretical point of view, highly precise methods exploiting the axial symmetry of these molecules can further be employed as a basis for two-or-more-electron systems as, for example, for studying the ro-vibrational photodissociation of the HeH^+ molecule [31–33].

The HeH^{2+} molecule, which is the system studied in this contribution, has a number of interesting electronic properties. Its ground electronic state ($1s\sigma$) potential energy surface (PES) does not possess a minimum, such that the molecule dissociates right away in this state. In contrast, the first excited state ($2p\sigma$) shows a metastable potential minimum (with the lifetime of 3.9 ns [34]). The equilibrium atom-atom separation of $R = R_0 = 3.89$ a.u. $\simeq 2.06$ Å [35,36] is twice as large as for the H_2^+ molecule and thus requires only one-fourth of the photoelectron energy to achieve the same interference effects.

Our goal is to analyze the asymmetry of the photoemission probability in the direction of the hydrogen or the helium atom, respectively. Such asymmetries have also been observed for homonuclear systems (due to the Fano resonance of competing channels) and exploited for probing molecular wave-packet dynamics [16]. We demonstrate how the impact of the Young-type interference to the PAD can be related to the nuclear dynamics of the HeH^{2+} molecule upon optimized laser-induced electronic transitions, including the reconstruction of the dissociative wave functions (Sec. III). The latter becomes possible because of the rich information encoded in the PAD (compared to angle-independent quantities like the total photoabsorption cross section). Large-scale numerical studies of the coupled electron and nuclear and laser field degrees of freedom are accomplished by invoking the renormalized Numerov method [37], which we have employed for computing accurate bound states of large fullerene molecules in

*jamal.berakdar@physik.uni-halle.de

previous studies [38]. We have extended the method (presented in Sec. II) to efficiently deal with unbounded states, making it well suited for a variety of scattering problems. We adopt atomic units consistently throughout the text.

II. COMPUTATIONAL METHODS

Invoking the adiabatic approximation, the wave function in the combined electronic and nuclear Hilbert space can be expanded as [39]

$$\Psi(\mathbf{r},R,t)=\sum_{\alpha}\chi_{\alpha}(R,t)\psi^{(\alpha)}(\mathbf{r};R), \tag{1}$$

where α labels electronic states parametrically dependent on the interatomic distance R. Inserting Eq. (1) into the time-dependent Schrödinger equation (TDSE) with the Hamiltonian [39]

$$\begin{aligned}H(t)&=H_0+V(t)=T_{\mathrm{c}}(R)+T_{\mathrm{e}}(\mathbf{r})+V_{\mathrm{ec}}(\mathbf{r},R)+V_{\mathrm{cc}}(R)\\&\quad+V_{\mathrm{el}}(\mathbf{r},t)+V_{\mathrm{cl}}(R,t)\end{aligned} \tag{2}$$

and projecting out the electronic part yields a standard coupled-channel evolution equation,

$$i\partial_t\ \chi_{\alpha}(R,t)=\sum_{\beta}\langle\psi^{(\alpha)}|H(t)|\psi^{(\beta)}\rangle\chi_{\beta}(R,t). \tag{3}$$

The first two terms in Eq. (2) describe the kinetic energy of the cores and electrons, respectively, whereas the next two terms stand for the Coulombic electron-core and the core-core interactions. Remaining time-dependent terms represent the interaction of the particles with the laser field, which is treated on the level of the dipole interaction. The matrix element $\langle\psi^{(\alpha)}|H(t)|\psi^{(\beta)}\rangle$ in Eq. (3) (with the integration over $\mathbf{r}$ only) reads

$$\langle\psi^{(\alpha)}|H(t)|\psi^{(\beta)}\rangle=-\frac{1}{2\mu}\frac{d^2}{dR^2}\delta_{\alpha\beta}+\mathcal{E}_{\alpha\beta}(R)-\mathcal{D}_{\alpha\beta}(R)E(t), \tag{4}$$

where the first term corresponds to the kinetic energy $T_{\mathrm{e}}(R)$ of the two-nuclei system with the reduced mass μ and $\mathcal{E}_{\alpha\beta}(R)$ captures three other time-independent operators in Eq. (2), while $\mathcal{D}_{\alpha\beta}(R)$ describes the dipole elements and $E(t)$ the electric field. The adiabatic approximation ignores derivatives of the electronic wave functions with respect to R, such that $\mathcal{E}_{\alpha\beta}(R)$ become diagonal with the diagonal elements $\mathcal{E}_{\alpha}(R)$ fulfilling the purely electronic eigenvalue condition for fixed R. The validity of the adiabatic approximation is constrained by the energy separation between different PESs [given by the R-dependent eigenvalues $\mathcal{E}_{\alpha}(R)$]. Hence, a modification of this scheme becomes necessary in the vicinity of avoided crossings.

A. Electronic states

As outlined above, finding the electronic eigenstates $\psi^{(\alpha)}$ for all (fixed) values of R is the basic ingredient for solving for the molecular dynamics. We expand the wave functions in terms of the spherical harmonics:

$$\psi^{(\alpha)}(\mathbf{r})=\sum_{\ell m}\frac{\phi^{(\alpha)}_{\ell m}(r)}{r}Y_{\ell m}(\hat{\mathbf{r}}). \tag{5}$$

Note that the dependence on R has been omitted for brevity. The origin of coordinate system is set at the geometric center of the molecule and the zenith is in the direction of the He atom. Inserting Eq. (5) into the Schrödinger equation yields the coupled-channel eigenvalue equation

$$\sum_{\ell' m'}\left[-\frac{1}{2}\frac{d^2}{dr^2}\delta_{\ell\ell'}\delta_{mm'}+V_{\ell m\ell' m'}(r)\right]\phi^{(\alpha)}_{\ell' m'}(r)=\mathcal{E}_{\alpha}\phi^{(\alpha)}_{\ell m}(r), \tag{6}$$

where $V_{\ell m\ell' m'}(r)=V_{\mathrm{cc}}(R)\delta_{\ell\ell'}\delta_{mm'}+\langle\ell m|V_{\mathrm{ec}}|\ell' m'\rangle$ is evaluated by expanding the Coulombic potentials in terms of Legendre polynomials followed by the Clebsch-Gordan algebra [40]. We note that the cylindrical symmetry of the molecule implies that the Hamiltonian is diagonal with respect to m, such that electronic states can be classified spectroscopically according to their phase change when rotating around the molecular axis.

In what follows, we represent all wave functions and operators by vectors and matrices which are spanned in the (ℓ,m) space (marked as bold face). Thus, Eq. (6) can be cast into a general multichannel form,

$$\left\{\frac{d^2}{dr^2}\mathbf{I}+2[\mathcal{E}\mathbf{I}-\mathbf{V}(r)]\right\}\boldsymbol{\phi}(r)=0. \tag{7}$$

The renormalized Numerov method [37] is then implemented as follows: The vector $\boldsymbol{\phi}(r)$ expressed as a product of the fundamental solution matrix $\boldsymbol{\Phi}(r)$ with a constant vector $\mathbf{c}$ (to be determined). The coordinate r is now represented by an equidistant grid with the step size h. The basic idea is to eliminate the wave-function-like quantity $\boldsymbol{\Phi}_n\equiv\boldsymbol{\Phi}(r_n)$ in favor of the ratio matrix $\mathbf{R}_n$ relating the function's values at adjacent grid points. Let us denote

$$\mathbf{T}_n=-\frac{h^2}{6}[\mathbf{I}\mathcal{E}-\mathbf{V}(r_n)]\quad\text{and}$$

$$\mathbf{U}_n=(\mathbf{I}-\mathbf{T}_n)^{-1}(2\mathbf{I}+10\mathbf{T}_n).$$

Applying Numerov's finite differences formula and substituting $\mathbf{F}_n=[\mathbf{I}-\mathbf{T}_n]\boldsymbol{\Phi}_n$, one finds

$$\mathbf{F}_{n+1}=\mathbf{R}_n\mathbf{F}_n, \tag{8}$$

where the ratio matrix obeys the recurrence relation,

$$\mathbf{R}_n=\mathbf{U}_n-\mathbf{R}_{n-1}. \tag{9}$$

Similar recursion relations can also be written for the backward propagation, as discussed in detail by Johnson [37]. Importantly, propagation of the ratio matrix is a very stable procedure, unlike working with the wave function itself. The benefits become evident in classically forbidden regions: Whereas the wave function contains an exponentially growing term that can possibly lower the precision, the ratio matrix varies only slowly. This can also be understood by the close relationship between the ratio matrix and the logarithmic derivative.

The energy eigenvalues are then found by choosing a matching point r_M and solving the recurrence relation Eq. (9) starting from the left and the right boundaries separately until r_M is reached. The continuity of the wave function and its first derivative at this point are the determining conditions for the energy eigenvalues. The search is performed by the Brent

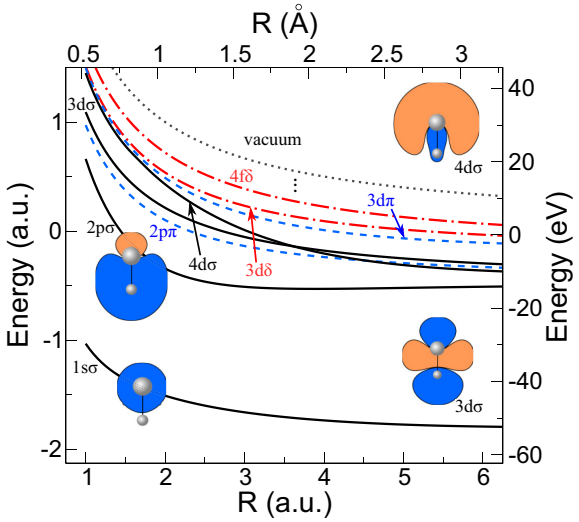

FIG. 1. (Color online) The PES of the first σ (solid black), π (dashed blue), and δ (dot-dashed red lines) states along with their spectroscopic labels of the HeH^{2+} molecule as a function of interatomic distance R. The insets depict a cut through the σ-molecular orbitals with a plane parallel to the molecular axis (at the equilibrium distance). Blue color indicates positive vales of $\psi^{(\alpha)}$ and orange negative values.

method for nondegenerate states and by the node-counting algorithm otherwise [38]. The actual wave function can easily be obtained from Eq. (8) once the energy is fixed.

Using the renormalized Numerov method, we have computed the first four eigenstates $\psi^{(\alpha)}(\mathbf{r};R)$ for $m=0$ and lowest energy states for $m=1,2$ for various values for R. The sum over ℓ in Eq. (5) has been truncated at $\ell_{\max}=24$, providing an accuracy of at least five digits for all eigenvalues. The PES $\mathcal{E}_\alpha(R)$ for these states is shown in Fig. 1, along with an orbital representation of the corresponding wave functions.

B. Scattering properties

In order to describe the photoemission from an (general) electronic state $|\psi_0\rangle$ (initial energy $\mathcal{E}_0$) within the weak-field approximation, an expansion in terms of the photon numbers proves to be particularly useful, which is nothing else but the Floquet series. Suppose the time-dependent Hamiltonian reads $H(t)=H_0+\{\delta H e^{-i\omega t}+\delta H^\dagger e^{i\omega t}\}$, the projection on the different laser-dressed states with a particular photon number N yields the Floquet hierarchy [41],

$$[\mathcal{E}_0+N\omega-H_0]|\psi_N\rangle=\delta H|\psi_{N-1}\rangle+\delta H^\dagger|\psi_{N+1}\rangle. \quad (10)$$

Note that the operator δH in Eq. (10) only allows for single-photon transitions. For low laser field intensity, Eq. (10) can be truncated at $N=1$, such that we obtain the inhomogeneous or *driven Schrödinger equation* (DSE),

$$[\mathcal{E}_0+\omega-H_0]|\psi^+\rangle=\delta H|\psi_0\rangle. \quad (11)$$

Here $|\psi^+\rangle$ denotes the first-order correction to the initial wave function upon the irradiation with the laser field. Equation (11) is consistent with the standard time-dependent perturbation theory [42]. Solving DSE (11) with *outgoing boundary conditions* [42] (the superscript + has been added for this reason) reproduces the scattering amplitude without the necessity of computing the transition matrix elements in perturbative treatments. Thus, it represents a very economical tool to study photoemission and related processes [43–45]. The only ingredient required is the asymptotic behavior of the scattering solution $|\psi^+\rangle$. For an electron subject to spherically symmetric short-range $V_{\rm sh}(r)$ and Coulomb Z/r potentials the asymptotic solution of Eq. (11) for a particular set (ℓ,m) of angular momentum quantum numbers reads

$$\psi^+_{\ell m}(\mathbf{r})\overset{V_{\rm sh}(r)\to 0}{\sim} i^{-\ell}e^{-i\sigma_\ell(k)}\mathcal{F}_{\ell m}(k)H^+_\ell(kr;\eta)Y_{\ell m}(\hat{\mathbf{r}}), \quad (12)$$

where $k=\sqrt{2(\mathcal{E}_0+\omega)}$ is the photoelectron momentum, $\sigma_\ell=\arg\Gamma(\ell+1+i\eta)$ the Coulomb phase shift, and $\eta=Z/k$ the Sommerfeld parameter. The Hankel function ([46], Sec. 32.2.11) $H^+_\ell(kr;\eta)=iF_\ell(kr;\eta)+G_\ell(kr;\eta)$ (where F_ℓ and G_ℓ are the regular and the irregular Coulomb functions, respectively) ensures the purely outgoing asymptotic properties. The scattering amplitude $\mathcal{F}_{\ell m}(k)$ includes all the scattering phase shifts from $V_{\rm sh}(r)$ and therefore completely determines the PAD.

For our specific case of the HeH^{2+} molecule, asymptotic solutions can also be easily constructed: At sufficiently large distances $r>r_C$ from the molecule the one-center approximation is valid and it suffices to take the first term $-3/r$ from the multipole expansion of the Coulomb potential. The outgoing wave takes a form of Eq. (12) with $Z=3$. A particular choice of r_C was found to have little influence on the final results, and we set $r_C=80$ a.u. as the cutoff distance.

In order to numerically determine for a given initial state $\psi_0(\mathbf{r})$ the yet unknown scattering amplitude $\mathcal{F}_{\ell m}(k)$, we generalize (similar to Ref. [48]) the renormalized Numerov method from Sec. II A to incorporate the driving term [cf. Eq. (11)]. This can easily be achieved by extending Eq. (8) to

$$\mathbf{F}_{n+1}=\mathbf{R}_n\mathbf{F}_n+\mathbf{b}_n, \quad (13)$$

with the ratio matrix $\mathbf{R}_n$ still obeying Eq. (9), whereas the additional vector $\mathbf{b}_n$ satisfies the recurrence relation

$$\mathbf{b}_n=\frac{h^2}{12}[\mathbf{s}(r_{n+1})+10\mathbf{s}(r_n)+\mathbf{s}(r_{n-1})]-\mathbf{R}^{-1}_{n-1}\mathbf{b}_{n-1}. \quad (14)$$

The function $\mathbf{s}(r)$ is the vector representation (with respect to the spherical harmonics) of $\delta H\psi_0(\mathbf{r})=-(\mathbf{E}_0\cdot\mathbf{r})\psi_0(\mathbf{r})$; i.e., it describes the interaction of the electron with linearly polarized light with the electrical field of amplitude $\mathbf{E}_0$ within the dipole approximation. Note that instead of propagating all linearly independent vectors spanning the space of possible initial derivatives as in Eq. (8), for the driven equation it is sufficient to start with already known bound state and, thus, propagate only *one* vector [Eq. (13)]. This is consistent with the loss of arbitrariness of the normalization in the case of DSE.

The numerical scheme now runs as follows. (i) Equations (9) and (14) are propagated from $r=0$ to $r=r_C$. This procedure yields $\mathbf{R}_C$ and $\mathbf{b}_C$. (ii) The scattering amplitude $\mathcal{F}_{\ell m}(k)$ can now be found by comparing $\mathbf{R}_C$ with known asymptotic solutions $\tilde{\mathbf{R}}_C$. As Eq. (12) demonstrates the ratio matrix $\tilde{\mathbf{R}}_C$ in the asymptotic limit does not mix different components; i.e., it is diagonal. Therefore, it can be constructed from the known asymptotic solution at two adjacent grid

points,

$$\tilde{\mathbf{R}}_C = \tilde{\mathbf{F}}_{C+1}\tilde{\mathbf{F}}_C^{-1} = [\mathbf{I} - \mathbf{T}_{C+1}]\mathrm{diag}\left\{\frac{H_\ell^+(kr_{C+1};\eta)}{H_\ell^+(kr_C;\eta)}\right\}_{\ell m}[\mathbf{I} - \mathbf{T}_C]^{-1}.$$

(iii) Imposing the continuity condition yields

$$\mathbf{F}_{C+1} = \tilde{\mathbf{R}}_C\mathbf{F}_C = \mathbf{R}_C\mathbf{F}_C + \mathbf{b}_C. \tag{15}$$

This equation makes it possible to determine $\mathbf{F}_C$ and thus the scattering wave function at r_C. The desired scattering amplitude $\mathcal{F}_{\ell m}(k)$ is then obtained by the comparison with Eq. (12).

Hence, the outlined procedure does not require exact scattering wave functions for the calculation of scattering amplitudes. Only a single outward propagation (for fixed photoelectron energy) is necessary to compute $\mathcal{F}_{\ell m}(k)$.

C. Diabatic representation

Figure 1 reveals the existence of a crossing point at $R_{\mathrm{cr}} = 3.595$ a.u. between the $\psi^{(3d\sigma)}$ and the $\psi^{(4d\sigma)}$ states, which is in fact an avoided crossing with a gap energy $\mathcal{E}_{4d\sigma}(R_{\mathrm{cr}}) - \mathcal{E}_{3d\sigma}(R_{\mathrm{cr}}) = 2.6467 \times 10^{-3} \simeq 72\,\mathrm{meV}$. The small energy separation hence necessitates a transformation from the adiabatic to the diabatic representation to account for the coupling of the two PESs. The adiabatic transition of the state $\psi^{(3d\sigma)}$ to $\psi^{(4d\sigma)}$ can be pictured by the upper negative (orange) lobe of the orbital corresponding to $\psi^{(3d\sigma)}$ (see Fig. 1) moving downwards, as the negative lobe is "squeezed" out to resemble the shape of $\psi^{(4d\sigma)}$. We determine the diabatic surfaces $\mathcal{E}_{ij}^{\mathrm{D}}(R)$, $i,j = 1,2$, by a simple interpolation technique; that is, we impose $\mathcal{E}_{11}^{\mathrm{D}}(R_{\mathrm{cr}}) = \mathcal{E}_{22}^{\mathrm{D}}(R_{\mathrm{cr}}) = [\mathcal{E}_{4d\sigma}(R_{\mathrm{cr}}) + \mathcal{E}_{3d\sigma}(R_{\mathrm{cr}})]/2$ and $\mathcal{E}_{11}^{\mathrm{D}}(R)[\mathcal{E}_{22}^{\mathrm{D}}(R)] \to \mathcal{E}_{3d\sigma}(R)[\mathcal{E}_{4d\sigma}(R)]$ as $|R - R_{\mathrm{cr}}|$ grows. The actual transformation is accomplished by the rotation

$$\mathcal{U}^\dagger(R)\begin{pmatrix}\mathcal{E}_{11}^{\mathrm{D}}(R) & \mathcal{E}_{12}^{\mathrm{D}}(R)\\ \mathcal{E}_{12}^{\mathrm{D}}(R) & \mathcal{E}_{22}^{\mathrm{D}}(R)\end{pmatrix}\mathcal{U}(R) = \begin{pmatrix}\mathcal{E}_{3d\sigma}(R) & 0\\ 0 & \mathcal{E}_{4d\sigma}(R)\end{pmatrix}, \tag{16}$$

where

$$\mathcal{U}(R) = \begin{pmatrix}\cos\Omega(R) & \sin\Omega(R)\\ -\sin\Omega(R) & \cos\Omega(R)\end{pmatrix}. \tag{17}$$

Together with the aforementioned conditions, solving Eq. (16) allows for interpolating $\Omega(R)$ and thus yields the diagonal and off-diagonal diabatic PESs. Once $\mathcal{U}(R)$ is known, calculations can be performed within the diabatic basis. Observables are computed by the corresponding backwards transformation.

All following calculations are carried out in cylindrical symmetry, as we take the laser polarization $\mathbf{E}_0$ along the molecular axis. Hence, the (not avoided) crossing of the σ orbitals with the $2p\pi$ state does not require special treatment as $\pi \leftrightarrow \sigma$ dipolar transitions are forbidden by the symmetry selection rules.

III. PUMP-PROBE INTERFERENCE SPECTROSCOPY

Within a simple LCAO model [49] for the initial states and plane waves (PWs) as the final states, the PAD takes the form

$$\frac{dP}{d\Omega} \propto (\boldsymbol{\epsilon}\cdot\mathbf{k})^2[A(\mathbf{k}) + B(\mathbf{k})\cos(\mathbf{k}\cdot\mathbf{R})], \tag{18}$$

where $\boldsymbol{\epsilon}$ denotes the polarization direction of the laser field, $\mathbf{k}$ is the photoelectron momentum, while $\mathbf{R}$ is a vector along the molecular axis with length R. The parameters $A(\mathbf{k})$ and $B(\mathbf{k})$ are determined by shape of orbitals in momentum space. The interference term in Eq. (18) suggests a close connection between the PAD and the molecular geometry, a dependence that can be exploited for tracing the nuclear dynamics. Additionally, the photoelectron energy can also be tuned, providing even more information. We stress that an accurate treatment of both the initial and moreover the final states is required for correct angular distributions [27]; projecting on PWs excludes a class of transition channels due to the wrong parity properties [30].

We invoke two approximations for the photoionization process: (i) the sudden approximation, that is, the photoelectron is not influenced by the molecule dynamics after the liberation, and (ii) the spectral resolution of laser pulse is fine enough to resonantly separate the different PESs. Under these assumptions, the PAD for the total state $\Psi_\alpha(\mathbf{r},R,t) = \chi_\alpha(R,t)\psi^{(\alpha)}(\mathbf{r};R)$ reads

$$\frac{dP_\alpha}{d\Omega d\mathbf{k}} = \int dR\left|\sum_{\ell m}(-i)^\ell e^{i\sigma_\ell(k)}\mathcal{F}_{\ell m}^{(\alpha)}(k;R)Y_{\ell m}(\hat{\mathbf{k}})\right|^2 n_\alpha(R,t), \tag{19}$$

where the scattering amplitude $\mathcal{F}_{\ell m}^{(\alpha)}(k;R)$ for an initial electronic state $\psi^{(\alpha)}$ is computed using the methods from Sec. II B. $n_\alpha(R,t) = |\chi_\alpha(R,t)|^2$ is the probability density of finding the NWP at the position R at time t when electronic state of the system is given by $\psi^{(\alpha)}$.

For utilizing the interference phenomenon to probe the molecule wave function, we take the laser polarization axis along the molecule axis and consider photoemission in a small cone around that direction. In this way, the emitted electrons are most likely influenced by *one* of the atoms as they propagate to infinity (Fig. 2). In order to follow the nuclear dynamics we propose to use a typical pump-probe scheme [18,19,50]: A femtosecond laser pulse induces electronic transitions that subsequently drive the vibrational or dissociative dynamics of the molecule. The latter is then probed by a short pulse that promotes the electron in a scattering state. The probe-pulse needs to contain a sufficient number of optical cycles in order to address the system resonantly. Varying the delay Δt between the two pulses then makes it possible to monitor the evolution of $n_\alpha(R,\Delta t)$. As the observable we chose the integrated probability to detect a photoelectron within the detector angle θ_{D} either in the forward or the backward direction (see Fig. 2):

$$P_\alpha^{\mathrm{F}} = \int_0^{2\pi} d\phi\int_0^{\theta_{\mathrm{D}}}\sin\theta\frac{dP_\alpha}{d\Omega d\mathbf{k}}, \tag{20a}$$

$$P_\alpha^{\mathrm{B}} = \int_0^{2\pi} d\phi\int_{\pi-\theta_{\mathrm{D}}}^{\pi}\sin\theta\frac{dP_\alpha}{d\Omega d\mathbf{k}}. \tag{20b}$$

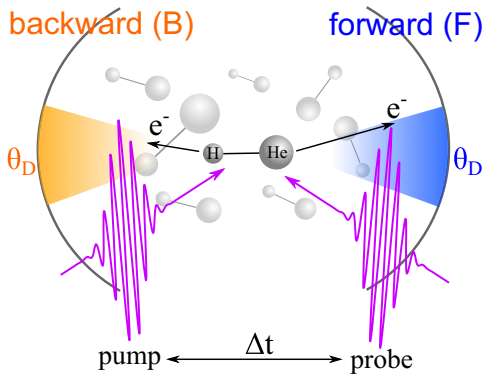

FIG. 2. (Color online) In the proposed setup for the pump-probe interference spectroscopy we only consider oriented molecules and allow for the photoelectron detection only within the acceptance angle θ_D. The time delay Δt between the pump and the probe pulses serves as the reference time for the induced dynamics.

In what follows we fix $\theta_D = 0.2\pi = 36^\circ$.

A. Interference profiles

Before we describe how the NWP dynamics triggered by the electronic excitation is reflected in the PAD, it is instructive to discuss the photoemission properties for a *fixed* geometry first [i.e., the averaging with respect to the nuclear wave function in Eq. (19) is ignored]. The forward (backward) emission probability P_α^{F} (P_α^{B}) for $1s\sigma$, $2p\sigma$, and $3d\sigma$ and $4d\sigma$ states is depicted in Figs. 3–5, respectively. The magnitude of the electrical field is set to $|\mathbf{E}_0| = 0.01$ a.u., which corresponds to an intensity of $\sim 3.5 \times 10^{12}$ W cm^{-2}. Conceptionally, the pulse is infinitely long; estimating, however, that the resonance condition is matched within ten optical cycles, the minimum temporal length is about 1.0 fs for the photoelectron energies studied here. Let us consider the photoemission from the $1s\sigma$ state first (Fig. 3). Depending on the energy of the photoelectron $\varepsilon_k = k^2/2$, the probability for the emission in the direction of the hydrogen atom shows an oscillatory behavior for varying R. In contrast, the emission in the He direction demonstrates only slight increase of probability with increasing R. These features are easily understood in terms of the wave function $\psi^{(1s\sigma)}$ (cf. the inset in Fig. 1). The helium atom carries most of the electron density; as $R \to \infty$ the electron becomes completely localized around its nucleus ($\mathrm{He}^+ + \mathrm{H}^+$). This density localization leads to an enhanced photoemission probability. On the other hand, the photoelectrons are not subject to any additional scattering when being emitted in the forward direction (i.e., no interference effects occur); interference effects come into play only for the backward (hydrogen) direction. The distance between the minima and the maxima is reduced with raising ε_k (as expected physically). The dependence is, in fact, square-root-like, but deficiencies of the explanation provided by the LCAO + PW model [Eq. (18)] become immediately apparent.

The situation is reversed for the $2p\sigma$ state (Fig. 4). Unlike the $1s\sigma$ state, the $2p\sigma$ PES asymptotically describes the dissociation into $\mathrm{H} + \mathrm{He}^{2+}$; i.e., the electron remains bound to the hydrogen atom. As a consequence, the photoemission in the backward direction is slightly larger than in the helium direction and shows more pronounced interference features. However, the localization of the electron density is not as strong as for the $1s\sigma$ state for the internuclear distance around the equilibrium value. Therefore, the forward emission is subject to the spatial interference as well. Even though the HeH^{2+} molecule lacks the inversion symmetry, certain parity effects that occur for inversion-symmetric systems (H_2^+, for example) can also be observed here. Comparing Fig. 4 to Fig. 3 shows a phase shift between the two sets of curves. If we

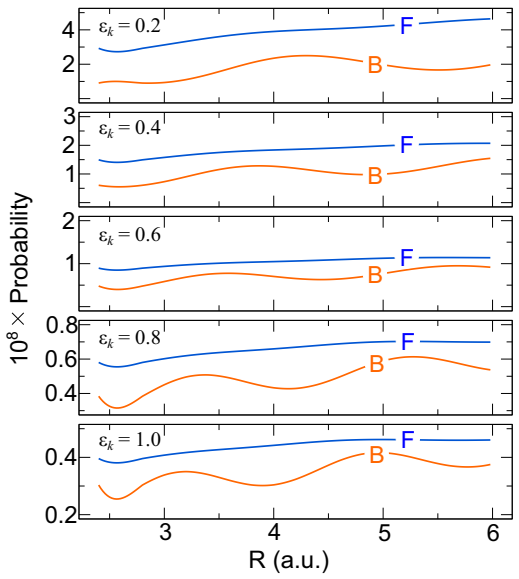

FIG. 3. (Color online) The emission probability $P_{1s\sigma}^{\mathrm{F}}$ (blue lines, marked with F) and $P_{1s\sigma}^{\mathrm{B}}$ (orange lines, marked with B) according to Eq. (20) for fixed values of R. The photoelectron energy ε_k is displayed in each panel.

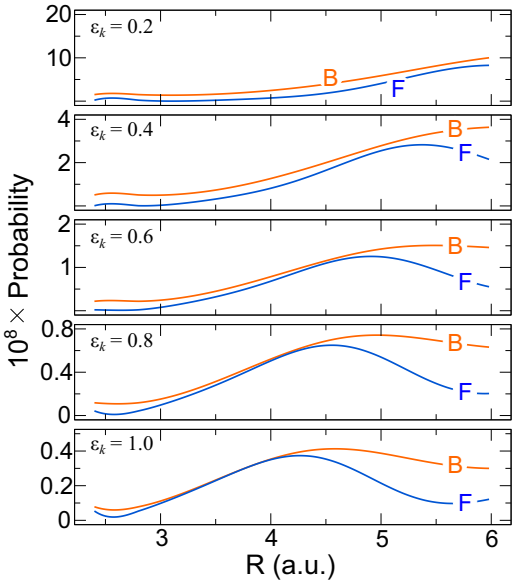

FIG. 4. (Color online) The emission probability $P_{2p\sigma}^{\mathrm{F}}$ (blue lines, marked with F) and $P_{2p\sigma}^{\mathrm{B}}$ (orange lines, marked with B) according to Eq. (20) for fixed values of R. The photoelectron energy ε_k is displayed in each panel.

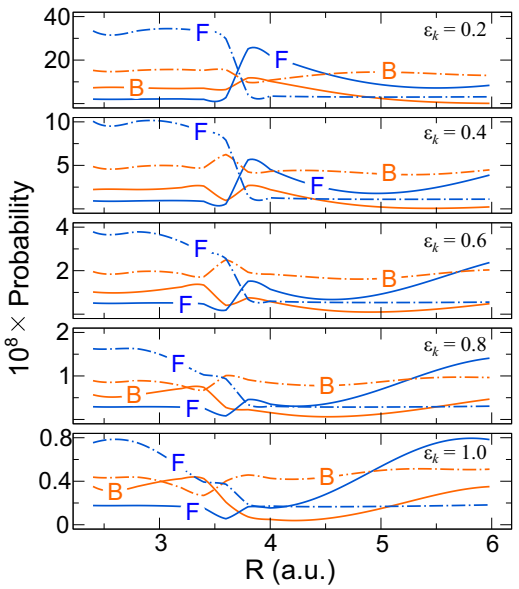

FIG. 5. (Color online) The emission probability P_α^{F} (blue lines, marked with F) and P_α^{B} (orange lines, marked with B) for the $3d\sigma$ (solid lines) and the $4d\sigma$ initial state (dot-dashed lines) for fixed values of R. The diabatic representation (Sec. II C) has been used to interpolate in the vicinity of the crossing point. The photoelectron energy ε_k is displayed in each panel.

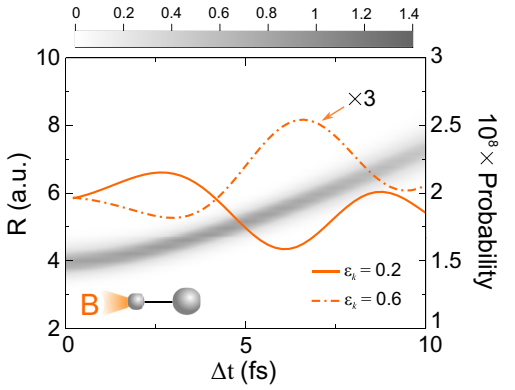

FIG. 6. (Color online) The NWP evolving in the PES $\mathcal{E}_{1s\sigma}$ after the pump pulse (see text). The grayscale map in the background depicts the NWP density $n_{1s\sigma}(R,\Delta t)$, while the overlaid graphs show the emission probability $P_{1s\sigma}^{\mathrm{B}}$ evaluated by Eq. (20) for $\varepsilon_k = 0.2$ a.u. (solid line) and $\varepsilon_k = 0.6$ a.u. (dot-dashed line). The latter has been multiplied by 3.0 to make it comparable with the solid line.

follow, for instance, the first maximum of $P_{1s\sigma}^{\mathrm{B}}$ upon increasing ε_k we notice that $P_{2p\sigma}^{\mathrm{F}}$ has an almost sine-like behavior at those R points. This is consistent with a phase change of the wave function from positive to negative values when going along the molecule axis (cf. Fig. 1). However, as the parity is not defined for HeH^{2+}, the explained dependence is only approximate.

The behavior of probability profiles for the $3d\sigma$ and the $4d\sigma$ states (Fig. 5) can be understood as a mixture of the profiles of the two lower states. For $R > R_{\mathrm{cr}}$, $P_{3d\sigma}^{\mathrm{F}}$ and $P_{3d\sigma}^{\mathrm{B}}$ are almost parallel, but with $P_{3d\sigma}^{\mathrm{F}} > P_{3d\sigma}^{\mathrm{B}}$. This becomes clear by noting that $\psi^{(3d\sigma)}$ is almost symmetrical with respect to the geometric center of the molecule (Fig. 1), while the majority of the localization probability is situated in the lower half. Interpreting the phase relation as for the $2p\sigma$ state is, however, not feasible since the electron emission can also take place the "middle" of the molecule and not only from the atom sites. The $4d\sigma$ state, on the other hand, has a node close to the position of the He atom, that is, positive and negative phase contributions close to each other that reduce the interference variations.

B. Nuclear-wave-packet dynamics

With the physical understanding of the interference phenomenon for photoionization of the σ states (Sec. III A) at our disposal, we can now draw our attention to the manifestation of the NWP dynamics. The molecule is assumed to be initially in the $\Psi_{2p\sigma}(\mathbf{r},R) = \chi_{2p\sigma}(R)\psi^{(2p\sigma)}(\mathbf{r};R)$ quantum state where $\chi_{2p\sigma}(R)$ is the nuclear *ground state* with respect to $\mathcal{E}_{2p\sigma}$ PES. With the laser polarization oriented *along* the molecule axis, the only possible excitation channels are the σ states. We solve Eq. (3) inserting a Gaussian-shaped pump laser pulse $E(t) = E_{\mathrm{pump}} e^{-(t-t_{\mathrm{m}})^2/2T_{\mathrm{p}}^2}\cos[\omega(t-t_{\mathrm{m}})]$ such that the central frequency ω matches the $2p\sigma \to 1s\sigma$ resonant transition at $R = R_0 = 3.89$ a.u. The pulse duration T_{p} was chosen to be as small as possible under the constraint that only the target PES lies in its spectral range. The laser amplitude was optimized to have the largest possible population transfer.

For transition $\psi^{(2p\sigma)} \to \psi^{(1s\sigma)}$ the pump field amplitude amounts to $E_{\mathrm{pump}} = 0.5$ a.u. (corresponds to peak intensity $I_{\mathrm{pump}} = 8.8\times10^{15}$ W cm^{-2}) and $T_{\mathrm{p}} = 0.5$ fs. With these parameters, the population transfer takes place in about 0.8 fs, a time scale on which the nuclear dynamics is basically frozen. For this reason, we present only the wave-packet dynamics after the population has been transferred; i.e., the origin of the time delay Δt (see Fig. 2) is set to 1.0 fs. As $\mathcal{E}_{1s\sigma}(R)$ is purely repulsive, the resulting wave-packet dynamics (Fig. 6) is dissociative.

Within 10 fs, the NWP moves outwards in an almost classical fashion (that is, the spreading remains approximately constant). Therefore, the expectation value $\langle\chi_{1s\sigma}(\Delta t)|R|\chi_{1s\sigma}(\Delta t)\rangle$ is a suitable quantity that can be compared to the interference profiles in Fig. 3. For $\varepsilon_k = 0.2$ a.u., the emission probability has a maximum around $R = 4.2$ a.u. and a minimum around $R = 5.5$ a.u., which can also be seen in Fig. 6, as the wave packet evolves. Taking $\varepsilon_k = 0.6$ a.u. instead turns the minimum (approximately) into a maximum, as present in Fig. 6, too. Hence, selecting certain values for the energy of the photoelectron makes it possible to focus on distinct regions in the R space where the photoemission is enhanced.

Even with optimal parameters, only about 90% of the ground-state population is transferred to the $1s\sigma$ state. Due to the R dependence of the transition matrix element and the energy separation, the remaining nuclear wave function $\chi_{2p\sigma}(R,\Delta t = 0)$ is (apart from having a smaller norm) shifted with respect to the vibronic ground state, launching a purely bound oscillatory dynamics (Fig. 7).

Within the region $3.0 < R < 5.0$, both the forward and the back emission probability have an almost linear slope for $\varepsilon_k = 0.4$ a.u. (see Fig. 4). Therefore, the detected signal is a good measure of the expectation value

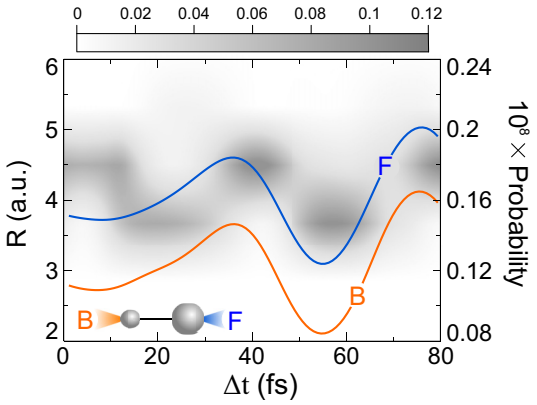

FIG. 7. (Color online) The NWP evolving in the PES $\mathcal{E}_{2p\sigma}$ after the pump pulse (see text). The grayscale map in the background depicts the nuclear wave function density $n_{2p\sigma}(R,\Delta t)$, while the overlayed graphs show the forward (blue) and backward (orange) emission probability according to Eq. (20). The photoelectron energy amounts to $\varepsilon_k = 0.4$.

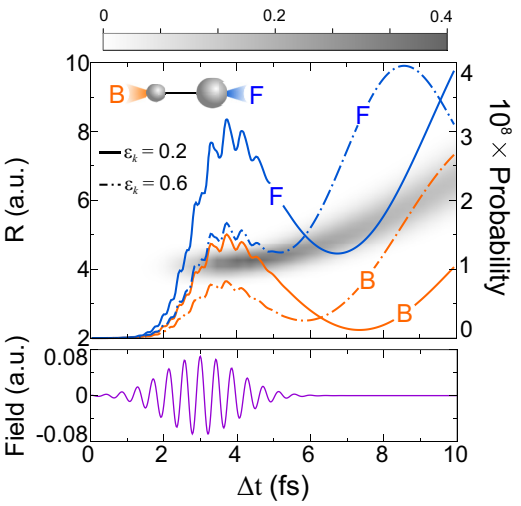

FIG. 8. (Color online) The electronic population and the NWP dynamics in the coupled-channel diabatic PES $\mathcal{E}^{\mathrm{D}}_{ij}$, $i,j = 1,2$ as functions of time. The grayscale map in the background depicts the nuclear wave function density $n_1(R,\Delta t)$ [which is identical to $n_{3d\sigma}(R,\Delta t)$ for $\Delta t \gtrsim 5$ fs], while the overlayed graphs show the forward (blue) and backward (orange) emission probability according to Eq. (20). The photoelectron energy amounts to $\varepsilon_k = 0.2$ a.u. (solid lines) and $\varepsilon_k = 0.6$ a.u. (dot-dashed lines).

$\langle\chi_{2p\sigma}(\Delta t)|R|\chi_{2p\sigma}(\Delta t)\rangle$, which should undergo a nearly harmonic time dependence. This is confirmed by Fig. 7 (overlaid graphs), which depicts $P^{\mathrm{F/B}}_{2p\sigma}$ as a function of Δt.

In order to target the $3d\sigma$ state instead one needs to account for a smaller energy separation between the PESs and correspondingly adjust the pump-pulse parameters. Because it is not possible to separately address $\psi^{(3d\sigma)}$ and $\psi^{(4d\sigma)}$ states, Eq. (3) is solved using the *diabatic* representation, taking $\omega = [\mathcal{E}^{\mathrm{D}}_{11}(R_0) + \mathcal{E}^{\mathrm{D}}_{22}(R_0)]/2$. We found that $T_{\mathrm{p}} = 1.0$ fs provides a good compromise between a fast transfer and sufficient spectral sharpness, while $E_{\mathrm{pump}} = 0.08$ a.u. ($I_{\mathrm{pump}} \simeq 2.2 \times 10^{14}$ W cm^{-2}) serves for an optimal population transfer. However, the electron remains with more than 70% probability in the $2p\sigma$ state. The transition can be imagined as "drilling" a Gaussian-shaped hole into the nuclear ground state, separating $\chi_{2p\sigma}(R,\Delta t)$ into an "inner" and an "outer" wave packet. The latter one is dissociating, whereas the inner wave packet performs small oscillations. Because both $3d\sigma$ and $4d\sigma$ PESs are strongly repulsive, the transferred wave packets quickly propagate out of the crossing region, and we can safely identify them with $\chi_{3d\sigma}(R,\Delta t)$ [or $\chi_{4d\sigma}(R,\Delta t)$] corresponding to the electronic state $\psi^{(3d\sigma)}$ (or $\psi^{(4d\sigma)}$). The majority of the population is found in the $3d\sigma$ state, which, similarly to Fig. 6, gives rise to a fast dissociation dynamics (Fig. 8). Since we can no longer regard the nuclei as frozen during the time when the pump field is switched on, Fig. 8 depicts the full dynamics starting from zero population in the $3d\sigma$ state. The time delay Δt is in this case measured from 3.0 fs before the peak field is reached (bottom panel in Fig. 8). The photoemission requires a sufficient separation between the initial states in order to be able to resolve them. Therefore, the population transfer dynamics for $\Delta t < 5$ fs in Fig. 8 cannot be observed in such an experiment (Fig. 8 only includes the $3d\sigma$ state). For $\Delta t > 5$ fs the NWP completely leaves the crossing region and can be treated within the *adiabatic* approximation. Again, we can pick certain values for ε_k in order to extract different features of the wave packet (see Fig. 5). Choosing $\varepsilon_k = 0.2$ a.u. allows for tracing the evolving wave function in the region around $R = 5.5$ a.u., where the emission probability shows a dip, and to observe the respective increase when moving outwards. Similarly, setting $\varepsilon_k = 0.6$ a.u. shifts the emission maximum in the forward direction to smaller values of R, such that the region around $R = 7$ a.u. is probed.

C. Nuclear-wave-packet reconstruction

The dependence of the photoemission probabilities on the photoelectron energy enables us to extract even richer information, provided the laser frequency ω can be tuned fine enough. We demonstrate here that not only certain expectation values, but the whole NWP density can be reconstructed from the mentioned energy dependence. This procedure works well when a bounded region where the wave packet is currently localized, can be estimated. This can be achieved by the analysis of Secs. III A and III B. Choosing ε_k such that the R dependence of the interference profiles is adequately described by a parabola, the corresponding photoemission probabilities with respect to a NWP $\chi_\alpha(R,t)$ allow for determining the expectation values of R and R^2, from which the width of the wave packet can be estimated. Once this is done, the function $n_\alpha(R,t) = |\chi_\alpha(R,t)|^2$ (for a fixed time) can be obtained by solving the integral equation corresponding to Eq. (19). We, however, found it more convenient to work with the relative forward photoemission rate

$$\widetilde{P}^{\mathrm{F}}_\alpha = \frac{P^{\mathrm{F}}_\alpha}{P^{\mathrm{F}}_\alpha + P^{\mathrm{B}}_\alpha} \tag{21}$$

instead, in order to eliminate the reduction of the probability for increasing ε_k. Equations (19) and (20) imply the integral

equation

$$\widetilde{P}^{\mathrm{F}}_{\alpha}(\varepsilon_k) = \int dR K^{\mathrm{F}}(\varepsilon_k, R) n_{\alpha}(R,t) \tag{22}$$

with a kernel

$$K^{\mathrm{F}}(\varepsilon_k, R) = \frac{\mathcal{P}^{\mathrm{F}}_{\alpha}(\varepsilon_k, R)}{\mathcal{P}^{\mathrm{F}}_{\alpha}(\varepsilon_k, R) + \mathcal{P}^{\mathrm{B}}_{\alpha}(\varepsilon_k, R)}. \tag{23}$$

The functions $\mathcal{P}^{\mathrm{F/B}}_{\alpha}$ in Eq. (23) are defined as

$$\mathcal{P}^{\mathrm{F}}_{\alpha}(\varepsilon_k, R) = \int_0^{2\pi} d\phi \int_0^{\theta_{\mathrm{D}}} d\theta \sin\theta \times \left| \sum_{\ell m} (-i)^{\ell} e^{i\sigma_{\ell}(k)} \mathcal{I}^{(\alpha)}_{\ell m}(k; R) Y_{\ell m}(\hat{\mathbf{k}}) \right|^2 \tag{24}$$

(and $\mathcal{P}^{\mathrm{B}}_{\alpha}$ analogously). In order solve Eq. (22) for the NWP density, we discretize the R coordinate (into N points) in the region $R_{\min} \leqslant R \leqslant R_{\max}$, where the wave packet is localized and approximate the integration (22) by the trapezoidal rule in order to obtain a system of M linear equations,

$$\widetilde{P}^{\mathrm{F}}_{\alpha}(\varepsilon_{k_i}) = \sum_{j=1}^{N} w_j K^{\mathrm{F}}(\varepsilon_{k_i}, R_j) n_{\alpha}(R_j, t), \quad i = 1, \ldots, M, \tag{25}$$

where the weights $w_1 = w_N = (R_{\max} - R_{\min})/2N$ and $w_j = (R_{\max} - R_{\min})/N$ otherwise. It is clear that we need $M \geqslant N$ values for ε_k to solve Eq. (25).

We have approximated the kernel Eq. (23) by a simple fifth-order polynomial in ε_k and R and computed $\widetilde{P}^{\mathrm{F}}_{\alpha}(\varepsilon_k)$ for $M = 40$ values for the photoelectron energy, distributed equidistantly in the interval $0.2 \leqslant \varepsilon_k \leqslant 1.0$. Solving Eq. (25) directly is, however, troublesome due to a nearly singular coefficient matrix $K^{\mathrm{F}}(\varepsilon_{k_i}, R_j)$. This problem can be avoided by reformulating Eq. (25) in terms of a minimization problem, where we have added a term suppressing oscillatory solutions. This leads to a numerically stable procedure for the reconstruction of the dissociative wave packets. A typical result is presented in Fig. 9. Unfortunately, finer structures could not be resolved, as can be seen, for instance, by $|\chi_{3d\sigma}(R, t = 4\ \mathrm{fs})|^2$ and the respective reconstructed density. However, more observables (possibly the complete PAD) can be added to the reconstruction algorithm to improve its accuracy. We propose it as a new technique for mapping NWP or to complement and support CE experiments.

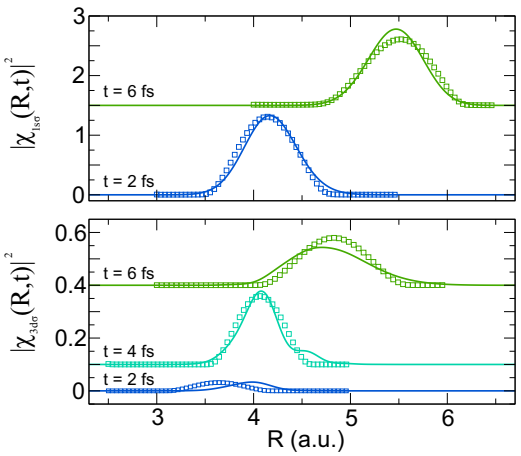

FIG. 9. (Color online) Comparison between the original NWP densities and the reconstruction for the $1s\sigma$ (top panel) and the $3d\sigma$ state (bottom panel) (see also Figs. 6 and 8) for different times. The solid lines are the original wave packets, whereas the squares in the corresponding color represent the reconstructed solutions. The curves for $t > 2$ fs have been shifted upwards for better visibility.

IV. CONCLUSIONS

In summary, a detailed study of the photoionization of the HeH^{2+} molecule in the weak-field regime has been performed. We have shown how the forward and backward photoemission rates (with respect to the molecular axis parallel to the laser polarization) depend on the interatomic distance and explained their oscillatory behavior by the interference effects. For the proposed pump-probe experimental setup we have computed the evolution of the NWP triggered by electron transitions (pump pulse) and its manifestation in the photoemission (probe pulse). Provided that the probe-pulse frequency can be tuned over a moderate energy range, the relative forward emission rate contains even more information and allows for reconstructing the NWP dynamics. Our proof-of-principle calculations demonstrate the feasibility of such an approach provided scattering cross sections can be precisely computed and measured.

ACKNOWLEDGMENTS

This work is supported by the DFG under Grants No. SFB762 and No. PA 1698/1-1. Consultation with R. Moshammer is gratefully acknowledged.

[1] T. Pfeifer, C. Spielmann, and G. Gerber, Rep. Prog. Phys. **69**, 443 (2006).
[2] E. Goulielmakis, M. Schultze, M. Hofstetter, V. S. Yakovlev, J. Gagnon, M. Uiberacker, A. L. Aquila, E. M. Gullikson, D. T. Attwood, R. Kienberger, F. Krausz, and U. Kleineberg, Science **320**, 1614 (2008).
[3] D. Shafir, Y. Mairesse, D. M. Villeneuve, P. B. Corkum, and N. Dudovich, Nat. Phys. **5**, 412 (2009).
[4] F. Krausz and M. Ivanov, Rev. Mod. Phys. **81**, 163 (2009).
[5] S. Haessler, J. Caillat, W. Boutu, C. Giovanetti-Teixeira, T. Ruchon, T. Auguste, Z. Diveki, P. Breger, A. Maquet, B. Carré, R. Taïeb, and P. Salières, Nat. Phys. **6**, 200 (2010).
[6] M. Schultze *et al.*, Science **328**, 1658 (2010).
[7] J. J. Rehr and R. C. Albers, Rev. Mod. Phys. **72**, 621 (2000).
[8] S. Pabst, Eur. Phys. J. Spec. Top. **221**, 1 (2013).
[9] H. D. Cohen and U. Fano, Phys. Rev. **150**, 30 (1966).
[10] E. Shigemasa, J. Adachi, M. Oura, and A. Yagishita, Phys. Rev. Lett. **74**, 359 (1995).

[11] X.-J. Liu, N. A. Cherepkov, S. K. Semenov, V. Kimberg, F. Gel'mukhanov, G. Prümper, T. Lischke, T. Tanaka, M. Hoshino, H. Tanaka, and K. Ueda, J. Phys. B **39**, 4801 (2006).
[12] B. Zimmermann, D. Rolles, B. Langer, R. Hentges, M. Braune, S. Cvejanovic, O. Geßner, F. Heiser, S. Korica, T. Lischke, A. Reinköster, J. Viefhaus, R. Dörner, V. McKoy, and U. Becker, Nat. Phys. **4**, 649 (2008).
[13] D. Akoury *et al.*, Science **318**, 949 (2007).
[14] M. Ilchen, L. Glaser, F. Scholz, P. Walter, S. Deinert, A. Rothkirch, J. Seltmann, J. Viefhaus, P. Decleva, B. Langer, A. Knie, A. Ehresmann, O. M. Al-Dossary, M. Braune, G. Hartmann, L. C. Tribedi, A. Meissner, M. AlKhaldi, and U. Becker, Phys. Rev. Lett. **112**, 023001 (2014).
[15] B. Fischer, M. Kremer, T. Pfeifer, B. Feuerstein, V. Sharma, U. Thumm, C. D. Schröter, R. Moshammer, and J. Ullrich, Phys. Rev. Lett. **105**, 223001 (2010).
[16] A. Fischer, A. Sperl, P. Cörlin, M. Schönwald, H. Rietz, A. Palacios, A. González-Castrillo, F. Martín, T. Pfeifer, J. Ullrich, A. Senftleben, and R. Moshammer, Phys. Rev. Lett. **110**, 213002 (2013).
[17] J. H. Posthumus, Rep. Prog. Phys. **67**, 623 (2004).
[18] M. Gruebele and A. H. Zewail, J. Chem. Phys. **98**, 883 (1993).
[19] A. H. Zewail, J. Phys. Chem. A **104**, 5660 (2000).
[20] A. D. Bandrauk and S. Chelkowski, Phys. Rev. Lett. **87**, 273004 (2001).
[21] S. Chelkowski and A. D. Bandrauk, Phys. Rev. A **65**, 023403 (2002).
[22] S. Barmaki and H. Bachau, J. Phys. B **40**, 463 (2007).
[23] M. Lein, J. Phys. B **40**, R135 (2007).
[24] H. Stapelfeldt, E. Constant, and P. B. Corkum, Phys. Rev. Lett. **74**, 3780 (1995).
[25] M. Magrakvelidze, O. Herrwerth, Y. H. Jiang, A. Rudenko, M. Kurka, L. Foucar, K. U. Kühnel, M. Kübel, N. G. Johnson, C. D. Schröter, S. Düsterer, R. Treusch, M. Lezius, I. Ben-Itzhak, R. Moshammer, J. Ullrich, M. F. Kling, and U. Thumm, Phys. Rev. A **86**, 013415 (2012).
[26] J. Colgan, A. Huetz, T. J. Reddish, and M. S. Pindzola, J. Phys. B **41**, 085202 (2008).
[27] R. D. Picca, P. D. Fainstein, M. L. Martiarena, and A. Dubois, J. Phys. Conf. Ser. **141**, 012006 (2008).
[28] R. Della Picca, P. D. Fainstein, and A. Dubois, Phys. Rev. A **84**, 033405 (2011).
[29] G. L. Yudin, S. Patchkovskii, and A. D. Bandrauk, J. Phys. B **39**, 1537 (2006).
[30] X. Guan, E. B. Secor, R. C. DuToit, and K. Bartschat, Phys. Rev. A **86**, 053425 (2012).
[31] H. B. Pedersen, S. Altevogt, B. Jordon-Thaden, O. Heber, M. L. Rappaport, D. Schwalm, J. Ullrich, D. Zajfman, R. Treusch, N. Guerassimova, M. Martins, J.-T. Hoeft, M. Wellhöfer, and A. Wolf, Phys. Rev. Lett. **98**, 223202 (2007).
[32] J. Loreau, J. Lecointre, X. Urbain, and N. Vaeck, Phys. Rev. A **84**, 053412 (2011).
[33] D. Ursrey, F. Anis, and B. D. Esry, Phys. Rev. A **85**, 023429 (2012).
[34] I. Ben-Itzhak, Z. Chen, B. D. Esry, I. Gertner, O. Heber, C. D. Lin, and B. Rosner, Phys. Rev. A **49**, 1774 (1994).
[35] I. Ben-Itzhak, I. Gertner, O. Heber, and B. Rosner, Phys. Rev. Lett. **71**, 1347 (1993).
[36] H. Miyagi, T. Morishita, and S. Watanabe, Phys. Rev. A **85**, 022708 (2012).
[37] B. R. Johnson, J. Chem. Phys. **69**, 4678 (1978).
[38] Y. Pavlyukh and J. Berakdar, Phys. Rev. A **81**, 042515 (2010).
[39] R. Schinke, *Photodissociation Dynamics: Spectroscopy and Fragmentation of Small Polyatomic Molecules* (Cambridge University Press, Cambridge, UK, 1995).
[40] A. R. Edmonds, *Angular Momentum in Quantum Mechanics* (Princeton University Press, Princeton, NJ, 1996).
[41] G. W. F. Drake, *Springer Handbook of Atomic, Molecular, and Optical Physics* (Springer, Berlin, 2006).
[42] C. J. Joachain, *Quantum Collision Theory* (North-Holland, Amsterdam, 1975).
[43] C. W. McCurdy, M. Baertschy, and T. N. Rescigno, J. Phys. B **37**, R137 (2004).
[44] M. Baertschy, T. N. Rescigno, W. A. Isaacs, X. Li, and C. W. McCurdy, Phys. Rev. A **63**, 022712 (2001).
[45] D. M. Mitnik, G. Gasaneo, and L. U. Ancarani, J. Phys. B **46**, 015202 (2013).
[46] DLMF, *NIST Digital Library of Mathematical Functions*, http://dlmf.nist.gov/, Release 1.0.7 of 2014-03-21, online companion to [47].
[47] F. W. J. Olver, D. W. Lozier, R. F. Boisvert, and C. W. Clark (eds.), in *NIST Handbook of Mathematical Functions* (Cambridge University Press, New York, 2010), print companion to [46].
[48] M. L. Du, Comput. Phys. Commun. **77**, 229 (1993).
[49] R. McCarroll and B. L. Moiseiwitsch, Proc. Phys. Soc., London, Sect. A **70**, 507 (1957).
[50] M. Schüler, Y. Pavlyukh, and J. Berakdar, J. Phys. Chem. Lett. **4**, 1131 (2013).